Research article

Stefan Fossati, Simone Hageneder, Samia Menad, Emmanuel Maillart and Jakub Dostalek*

# Multiresonant plasmonic nanostructure for ultrasensitive fluorescence biosensing

https://doi.org/10.1515/nanoph-2020-0270
Received May 6, 2020; accepted July 11, 2020

**Abstract:** A novel metallic nanostructure for efficient plasmon-enhanced fluorescence readout of biomolecular binding events on the surface of a solid sensor chip is reported. It is based on gold multiperiod plasmonic grating (MPG) that supports spectrally narrow plasmonic resonances centered at multiple distinct wavelengths. They originate from diffraction coupling to propagating surface plasmons (SPs) forming a delocalized plasmonic hotspot associated with enhanced electromagnetic field intensity and local density of optical states at its surface. The supported SP resonances are tailored to couple with the excitation and emission transitions of fluorophores that are conjugated with the biomolecules and serve as labels. By the simultaneous coupling at both excitation and emission wavelengths, detected fluorescence intensity is enhanced by the factor of 300 at the MPG surface, which when applied for the readout of fluorescence immunoassays translates to a limit of detection of 6 fM within detection time of 20 min. The proposed approach is attractive for parallel monitoring of kinetics of surface reactions in microarray format arranged on a macroscopic footprint. The readout by epi-fluorescence geometry (that inherently relies on low numerical aperture optics for the imaging of the arrays) can particularly take advantage of the reported MPG. In addition, the proposed MPG nanostructure can be prepared in scaled up means by UV-nanoimprint lithography for future practical applications.

**Keywords:** fluorescence; multidiffractive gratings; optical biosensor; plasmonics; ultrasensitive assays.

***Corresponding author: Jakub Dostalek,** Biosensor Technologies, Austrian Institute of Technology GmbH, Konrad-Lorenz-Straße 24, Tulln 3430, Austria; and FZU-Institute of Physics, Czech Academy of Sciences, Na Slovance 2, Prague 182 21, Czech Republic. E-mail: Jakub.Dostalek@ait.ac.at. https://orcid.org/0000-0002-0431-2170

**Stefan Fossati and Simone Hageneder:** Biosensor Technologies, Austrian Institute of Technology GmbH, Konrad-Lorenz-Straße 24, Tulln 3430, Austria, E-mail: Stefan.Fossati@ait.ac (S. Fossati), Simone.Hageneder@ait.ac.at (S. Hageneder). https://orcid.org/0000-0002-1109-0035 (S. Fossati)

**Samia Menad and Emmanuel Maillart:** Horiba France SAS, 14, Boulevard Thomas Gobert - Passage Jobin Yvon CS 45002, Palaiseau 91120, France, E-mail: samia.menad@gmail.com (S. Menad), emmanuel.maillart@horiba.com (E. Maillart)

## 1 Introduction

In a variety of optical biosensors, plasmonic nanomaterials become routinely employed for direct label-free analysis of biomolecules based on the measurement of specific binding-induced refractive index changes [1, 2]. In addition, we witness rapid progress in the implementation of plasmonic nanomaterials for the amplification of weak optical spectroscopy signal in other biosensor modalities relying on fluorescence, Raman scattering, and infrared absorption spectroscopy [3–5].

Plasmon-enhanced fluorescence (PEF) spectroscopy takes advantage of the increased intensity and local density of optical states accompanied with the resonant excitation of surface plasmons (SPs). These resonances originate from collective oscillations of electron density and associated electromagnetic field at the surface of metallic nanostructures. The coupling of SPs with fluorophores allows their lifetime, quantum yield, excitation rate, and far-field angular distribution of the emitted light to be effeciently manipulated [6–8]. These phenomena can be tailored to enhance the sensitivity of fluorescence-based assays where fluorophores are used as labels. Then, plasmonic nanostructures are deployed at the sensor surface to increase the signal-to-noise ratio of detected fluorescence signal that is attributed to the capture of the target analyte from the analyzed liquid sample. In general, detected fluorescence intensity can be enhanced by the combined coupling of SPs with fluorophores at their absorption $\lambda_{ab}$ and emission $\lambda_{em}$ wavelengths [9, 10]. This interaction can (i) increase the excitation rate at $\lambda_{ab}$, (ii) improve extraction yield of fluorescence light from the sensor surface by narrowing the angular emission range at $\lambda_{em}$ towards the detector, and (iii) enhance quantum yield. The fact that the coupling with SPs occurs locally within their confined near-field allows only

the fluorescence signal emitted in the close proximity to the sensor surface without increasing the background signal originating from the bulk to be selectively amplified.

The coupling of SPs with fluorophores scales with their near-field intensity strength, which is limited by Ohmic losses causing damping. Metallic nanostructures supporting SPs with decreased damping can provide stronger near-field intensity enhancement, which manifests itself as a spectrally narrower surface plasmon resonance (SPR) [11–13]. However, if the spectral window where SPs are resonantly excited becomes narrower than the Stokes shift of the used fluorophores, the combined coupling at absorption $\lambda_{ab}$ and emission $\lambda_{em}$ bands is not possible, potentially leading to a decrease of fluorescence enhancement.

Metallic nanoparticles supporting localized surface plasmons (LSPs) typically exhibit spectrally broad resonances that can be tuned to spectrally overlap with both $\lambda_{ab}$ and $\lambda_{em}$ of commonly used organic fluorophores [14]. This, however, holds true only for isolated or randomly arranged metallic nanoparticles, where the excitation of LSPs with an optical wave traveling from the far-field is weakly angular dependent. Periodic arrangement of nanoparticles allows narrowing SPR spectral bands by diffraction coupling of LSPs on individual nanoparticles giving rise to delocalized lattice modes that exhibit sharp dispersive spectral features [11, 12, 15–17]. A wide range of such nanoparticle architectures has been developed to control fluorescence [18–21], allowing the detection of even single molecules [22]. These systems nevertheless are typically suitable for research, and their utilization to practical applications is hampered by the requirement of nanoscale control of emitter placement at the metallic nanoparticle and complex techniques needed for their manufacturing. Besides LSPs, propagating surface plasmon (PSP) modes can be excited on continuous metal films. They exhibit less confined near-field profile compared to LSPs and are dispersive over a broad spectral range. When interacting with fluorophores, the dispersive nature of PSPs can be even exploited to angularly separate emission from fluorophores exhibiting different $\lambda_{em}$ to distinct angles in the far-field by using the SP-coupled emission [23]. On continuous metal films, periodic corrugation can provide additional momentum in order to diffraction phase-match optical waves propagating in the far field with PSPs. These Bloch-like modes are delocalized along the surface with angular dispersive and narrow spectral characteristics, allowing the excitation of fluorophores at a certain angle, facilitating emission via PSPs, and outcoupling to propagating modes at different angles [24–26]. In order to overlap narrow plasmon resonances with multiple spectral windows, metallic nanoparticle assemblies supporting hybrid SP modes can be used [27, 28]. They are formed by the coupling of multiple metallic nanostructures, and architectures supporting both LSP and PSP modes have been studied [29, 30]. These systems support multiple hybrid SP modes at distinct wavelengths; however, they typically confine electromagnetic near-field intensity at different locations on the structure and thus do not allow for the simultaneous probing of species placed in their proximity at respective spectral windows.

Plasmonic nanostructures can be prepared by a range of lithography techniques providing different level of control over their properties. While large areas of homogeneous flat metallic films are easily prepared by vapor deposition techniques [31], their optical properties are mostly determined by the choice of material. Metal island films, often created by vapor deposition [32], can support LSP modes with local hotspots exhibiting broad size distribution and lack of order. Colloidal lithography techniques allow the preparation of domains with ordered patterns of metallic nanostructures [33]. Electron beam lithography is often employed to create almost arbitrary morphology of metallic nanostructures with high precision [34]. However, it is still considered as complex and not well suited for cost-efficient large-scale production. Laser interference lithography (LIL), a method where interference pattern formed by overlapping coherent light beams is transferred to a photosensitive material, allows us to quickly and relatively inexpensively structure large areas with periodic corrugation such as holographic gratings, nanohole, or nanoparticle arrays [35, 36].

Nanoimprint lithography (NIL) represents another promising approach to address scalability in nanofabrication. Molds carrying a structure that can be prepared by more complex methods are then employed to repeated transfer of the target motives into an imprint resist [37]. The precise replication of patterns with feature size below 20 nm [38] paved the way towards the application in modern semiconductor manufacturing. In parallel, high-throughput NIL methods are developed to produce nanostructured surfaces, even on flexible substrates [39].

Herein, we report a new approach to plasmonic nanostructures supporting multiple tunable resonances with delocalized plasmonic hotspot along the surface and we tailor them for the simultaneous coupling with fluorophores at both their absorption and emission bands. It is based on multiperiod plasmonic gratings (MPGs) that are engineered to diffractively couple near-field SP field to far-field optical waves traveling at desired wavelengths and directions. The optical surfaces are prepared by UV-LIL that is combined with UV-NIL in order to open the door for potential scaled up preparation. The developed type of

MPGs is particularly beneficial for fluorescence biosensors with array detection format and *in situ* readout of reaction kinetics that relies on inherently low numerical aperture optics for the excitation and collecting of fluorescence light. We show that the developed structure offers strong enhancement of fluorescence signal by a factor of 300, enables the monitoring of affinity binding that is not masked by the bulk signal, and, when applied to an immunoassay, allows rapid detection of the target analyte at concentrations as low as 6 fM on multiple spots in microarray format.

# 2 Materials and methods

## 2.1 Materials

Microscope slides made of BK7 glass were purchased from Carl Roth (Germany) and used as substrates. The positive photoresist MICROPOSIT S1805 G2 and its developer AZ303 were bought from Microresist (Karlsruhe, Germany), and the nanoimprint resist Amonil MMS10 was acquired from Amo GmbH (Berlin, Germany). The silicone kit DOWSIL Sylgard 184 was purchased from Conrad GmbH (Wels, Austria). Dithiols with carboxylic head group (SPT-0014A6, COOH-OEG6-dithiol) and oligoethylene glycol head group (SPT-0013, OH-OEG3-dithiol) were from SensoPath Technologies (Bozeman, MT, USA). Antimouse IgG conjugated with Alexa Fluor 790 (AF790) came from Thermo Fisher Scientific-Life Technologies (Eugene, OR, USA). Phosphate buffered saline (PBS), 1-ethyl-3-(3-dimethylaminopropyl) carbodiimide (EDC), N-hydroxysuccinimide (NHS), ethanolamine, Tween 20, bovine serum albumin (BSA) and purified mouse IgG were acquired from Sigma–Aldrich Handels-GmbH (Vienna, Austria).

## 2.2 Preparation of MPG nanostructures

UV-LIL [40] was employed for the preparation of MPG nanostructures. Briefly, a laser beam with $\lambda = 325$ nm was collimated and expanded in order to perform the recording over an area of 1 $cm^2$ with homogenous intensity of about 15 $\mu W/cm^2$. A glass or Si wafer substrate coated with a 500-nm thick film of positive photoresist S1805 was mounted into a Lloyd's mirror configuration to record sinusoidally modulated field intensity formed by the interference of two parts of the beam – one directly impinging at the resist layer and that other reflected by a UV mirror (Figure S1A). The period of the modulation $\Lambda$ was controlled by changing the angle of the interfering beams $\theta$. Multiple subsequent exposures of different periods $\Lambda$ were performed in order to yield the target structure. In this work, the exposure of the period of $\Lambda_1 = 564$ nm was followed by two additional orthogonal exposures carried out with an interference field period set to $\Lambda_2 = \Lambda_2 = 583$ nm. Between each recording step, the substrate with resist layer was rotated by an azimuthal angle $\varphi$ along the axis perpendicular to its surface. Next, the structure was etched into the photoresist by a developer and its topography was cast to polydimethylsiloxane (PDMS), which was used as a working stamp for the preparation of multiple copies by UV-NIL (Figure S1B). The PDMS was cured at room temperature for 48 h. For a small reduction of the pattern period, it is possible to cure the stamp at an elevated temperature of 60 °C. The thermal shrinking of the cured working stamp after the cooling to room temperature reduces the pattern period $\Lambda$ by about 1%. To prepare the plasmonic sensor chips by UV-NIL, glass slides were coated with a 130-nm layer of the nanoimprint resist Amonil MMS10, contacted with the working stamp, allowed to rest for 5 min, and were cured by UV cross-linker Bio-Link (Vilber Lourmat, Collégien, France) with 2 J $cm^{-2}$ irradiation dose at 365 nm (Figure S1C). The PDMS stamp was finally demolded, and the corrugated glass substrates with casted MPG topography on their top were subsequently coated with 4-nm-thick Cr and 100-nm-thick Au layers by vacuum thermal evaporation instrument Auto306 from HHV Ltd (Crawley, UK).

## 2.3 Characterization of MPG nanostructures

The topography of MPG nanostructures was studied with atomic force microscope PicoPlus from Molecular Imaging (Arizona, USA). The spectrum of PSP modes that are optically excited on the gold-coated MPG structures was observed from reflectivity measurements with the structure clamped against a transparent flow cell that was flooded with water. The polychromatic light beam of a halogen lamp was collimated, polarized with a Glan polarizer, and made impinging at the MPG structure. For a beam incident normal to the surface, a beam splitter cube (CCM1-BS013 from Thorlabs, New Jersey, USA) was used to separate the incident and reflected beams. The reflected light beam was collected by an optical fiber and brought at the input of a spectrograph (Shamrock 303i from, Andor, New York, USA). As a reference, a flat gold-coated glass substrate was used.

## 2.4 Sensor chip and surface modification

Immediately after the deposition of thin metallic layers, the substrates were incubated in an ethanolic thiol solution of 0.1 mM COOH-OEG6-dithiol and 0.9 mM OEG3-dithiol overnight in order to form a self-assembled monolayer (SAM). After rinsing with ethanol and drying with a stream of compressed air, the prepared samples were stored in argon atmosphere at room temperature until further use to ensure their stability over weeks [41].

## 2.5 Optical reader

Readout of the binding of biomolecules labeled by a fluorophore on the sensor chip with MPG nanostructure and the investigation of the enhancement strength provided by this nanostructure were carried out using a setup with epi-illumination fluorescence geometry. It was designed to image an area of 4 × 4 mm on the sensor chip with MPG at a scientific EM-CCD camera (iXon 885K from Andor, Belfast, UK) by the optical system with a numerical aperture of NA = 0.2. A monochromatic beam emitted from diode laser iBeam Smart 785S with $\lambda_{ex} = 785$ nm from TOptica, Photonics AG (Gräfelfing, Germany) passed through a laser cleanup filter (BP $\lambda_{ex}$, LL01-785 from Semrock, Rochester, NY, USA) and a spatial filter consisting of a 60× microscope objective, a 40 μm pinhole, and recollimation lens (lens 1, AC-254-40-B from Thorlabs, Newton, NJ, USA). The central part of the expanded and collimated beam was polarized (POL,

LPVIS100 from Thorlabs, Newton, NJ, USA) and directed towards the sample by a dichroic mirror (DM) module. It comprised a DM (Di02-R785 from Semrock, Rotchester, NY, USA) oriented by 45° with respect to the axis of the module, and its central area with 2-mm projected diameter was coated with 100-nm-thick gold serving as a central mirror (CM). The excitation beam at the wavelength of $\lambda_{ex}$ = 785 nm was focused at the CM by a lens (lens 2, AC-254-35-B from Thorlabs, Newton, NY, USA), and the reflected beam was recollimated with another lens (lens 3, AC-254-40-B from Thorlabs, Newton, NJ, USA). The collimated excitation beam was made normally incident at the sensor chip surface that carried MPG nanostructure. The distance between the DM module and the sensor chip was set to the focal distance of lens 3. In this configuration, the reflected excitation beam $\lambda_{ex}$ was focused again at the CM and reflected away from the detector arm. Contrary to the excitation beam $\lambda_{ex}$, the fluorescence light emitted from the sensor chip surface at longer wavelength $\lambda_{em}$ propagated at deviated angles and thus the majority of its intensity passed through the DM module towards the detector. The surface of the sensor chip was imaged at the detector plane by an imaging lens (lens 4, AC-254-80-B from Thorlabs, Newton, NJ, USA). In the detector arm, a notch filter (NF03-785E-25 from Semrock, Rotchester, NY, USA) and a fluorescence bandpass filter (FF01-810/10-25 from Semrock, Rotchester, NY, USA) were used to suppress the intensity of the excitation beam that leaked through the dichroic filter with the CM. Fluorescence images were acquired with a scientific EM-CCD camera operated at –70 °C and with EM gain set to 100. In-house-developed LabView software (LabView 2015, NI, Austin, TX, USA) was used to acquire image series and it comprised the data processing for determining the average signals on arrays of preselected spots and their progression over time.

### 2.6 Bioassay

For testing the analytical performance that is advanced by using sensor chips with the MPG nanostructure, a transparent flow cell was clamped on their top and the assembly was loaded to an optical fluorescence reader system. The flow cell consisted of a fused silica glass substrate with drilled input and output ports and a thin gasket cut from a 100-µm-thick PDMS sheet. The volume of the used flow chamber defined by the PDMS gasket was of several microliters, and aqueous samples were transported through the flow cell by using a peristaltic pump (from Isamtec, Switzerland).

The sensor chip carried a gold layer modified by a thiol SAM with carboxyl (COOH) and oligoethylene glycol (OEG) groups. In order to covalently couple protein ligands carrying amine groups, the COOH moieties on the thiol SAM were activated by a flow of an aqueous solution with 75 mg $mL^{-1}$ EDC and 21 mg $mL^{-1}$ NHS for 15 min. After rapid rinsing with acetate buffer of pH 4, mouse IgG dissolved (protein ligand) at a concentration of 50 µg $mL^{-1}$ in acetate buffer was flowed through the sensor and allowed to react with the gold sensor chip surface for around 90 min. The unreacted COOH groups were passivated by a 1 M ethanolamine solution in $H_2O$, adjusted to pH 8.5. Immediately after the functionalization step, the sensor chip was used for the readout of model bioassay and liquid samples with increasing concentration of antimouse IgG conjugated with AF790 were sequentially flowed through the sensor (incubation time of 15 min for each concentration, followed by a rinsing step with buffer). All assay components were dissolved in PBS containing 0.05% Tween 20 and 1 mg $mL^{-1}$ BSA.

### 2.7 Numerical simulations

The finite-difference time-domain method implemented in commercial software was employed from Lumerical Inc. (Canada). Optical near-field calculation of the electric field intensity distribution was performed at a wavelength that is coincident with the absorption band of the chosen emitter ($\lambda$ = 785 nm). Fluorophore emission was studied by representing a fluorophore as an oscillating electric dipole. Both absorption $\vec{\mu}_{ab}$ and emission $\vec{\mu}_{em}$ dipoles were assumed randomly oriented, and the respective optical response was averaged over all their possible orientation and locations on the surface. A computation cell was defined with lateral dimensions of 20 × 20 µm along the structure surface and height of 8 µm was used. Perfectly matched layer boundary conditions were applied to all boundaries. Cartesian coordinates were used and the axes in the plane of the structure are noted perpendicular (⊥) and parallel (||) and the axis perpendicular to the structure as $z$. The emitter was placed 15 nm above the gold corrugated surface in the $z$ direction. The wavelength-dependent refractive index of gold $n_m$ was modeled by fitting a Drude-Lorentz model to data from the CRC Handbook on Chemistry and Physics while the refractive index of water as bulk medium was assumed nondispersive with $n_s$ = 1.332. To study the spectrum of supported plasmonic modes, the MPG structure was illuminated with a plane wave source from above the bulk dielectric with refractive index $n_s$. Monitor planes were used 300 nm below and 700 nm above the surface to record the electrical field and calculate transmission and reflectivity. Furthermore, far-field distribution of the fluorescence emission in epi-fluorescence configuration was calculated by applying a far-field transformation to the reflectivity monitor.

## 3 Theory and experiment

The concept of MPG was pursued for the enhancement of fluorescence signal by using corrugation of a thin metal film with several encoded superimposed periodic modulations. These modulation components enable the precise design of the spectrum of excited plasmonic modes with

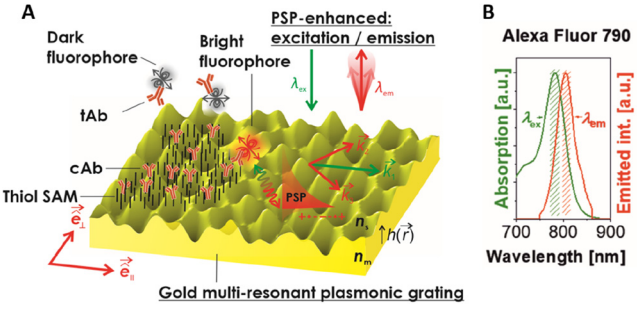


**Figure 1:** Concept of the MPG-based sensor readout. (A) Schematics of the surface of multiresonant MPG structure that carries a biointerface on its top to affinity capture fluorophore-labeled biomolecules that are probed by surface plasmon modes at its excitation and emission wavelengths. (B) Example of the absorption and emission spectra for selected fluorophore Alexa Fluor 790.

respect to the characteristics of the used fluorophores. Further, the structure was tailored for the amplification of fluorescence assays that utilize a near-infrared (NIR) fluorophore Alexa Fluor 790 (AF790) as a label. The MPG, schematically shown in Figure 1A, was implemented with grating periods suitable to resonantly excite PSPs on its surface at wavelengths that coincide with the excitation wavelength $\lambda_{ex}$ = 785 nm and emission wavelength $\lambda_{em}$ = 810 nm of A790 (see respective absorption and emission peaks in Figure 1B). In the NIR wavelength range, the resonant excitation of PSPs at regular gold grating surfaces is manifested as a spectral dip in the reflectivity spectrum with a width of about $\Delta\lambda_{FWHM}$ = 15 nm, which is substantially narrower than the Stokes shift of available fluorophore labels (including that for the chosen AF790 with $\lambda_{em}$–$\lambda_{ab}$ = 23 nm). Therefore, the MPG was developed in order to support two distinct plasmonic resonances that provide enhanced intensity of PSP field at both excitation and emission wavelengths of AF790 in order to locally increase the excitation rate (at $\lambda_{ex}$) and take advantage of SP-mediated emission with diffractive outcoupling of fluorescence light trapped by PSPs (at $\lambda_{em}$) towards the detector. The importance of these contributions to amplify the measured fluorescence intensity is experimentally and theoretically demonstrated, and it is utilized for ultrasensitive fluorescence-based detection of biomolecules.

## 3.1 Topography of MPG structure

The MPG structure with three superimposed periodic corrugations was investigated and prepared by UV-LIL. A thin photoresist layer was sequentially exposed to series of sinusoidal patterns formed by two coherent interfering plane waves, and the final corrugation structure was yielded by its etching. The first recording of a shorter period $\Lambda_1$ = 563 nm was followed by two additional longer periods $\Lambda_2$ = $\Lambda_3$ = 586 nm that were rotated around the axis perpendicular to the surface by an azimuthal angle of $\varphi$ = 45° and −45° (see Figure S1A). The superimposed interference field pattern is simulated in Figure 2A, and the respective etched corrugation profile can be described as the following height dependence:

$$h\left(\vec{r}\right) = \sum_{i=1}^{3} a_i \sin\left(\frac{2\pi}{\Lambda_i}\vec{\hat{k}}_i \cdot \vec{r}\right), \quad (1)$$

where $a_i$ is the amplitude, $\Lambda_i$ is the period of corrugation components, $\vec{\hat{k}}_i$ is the unit vector defining its orientation in the MPG plane ($i$ = 1, 2, 3), and $\vec{r}$ is the distance in the plane of the structure. Multiple substrates with identical corrugation profile were prepared by UV-NIL and coated with a 100-nm-thick Au film by vacuum thermal evaporation (Figure S1C). Atomic force microscopy was used to determine the topography of the prepared MPG, and the maximum

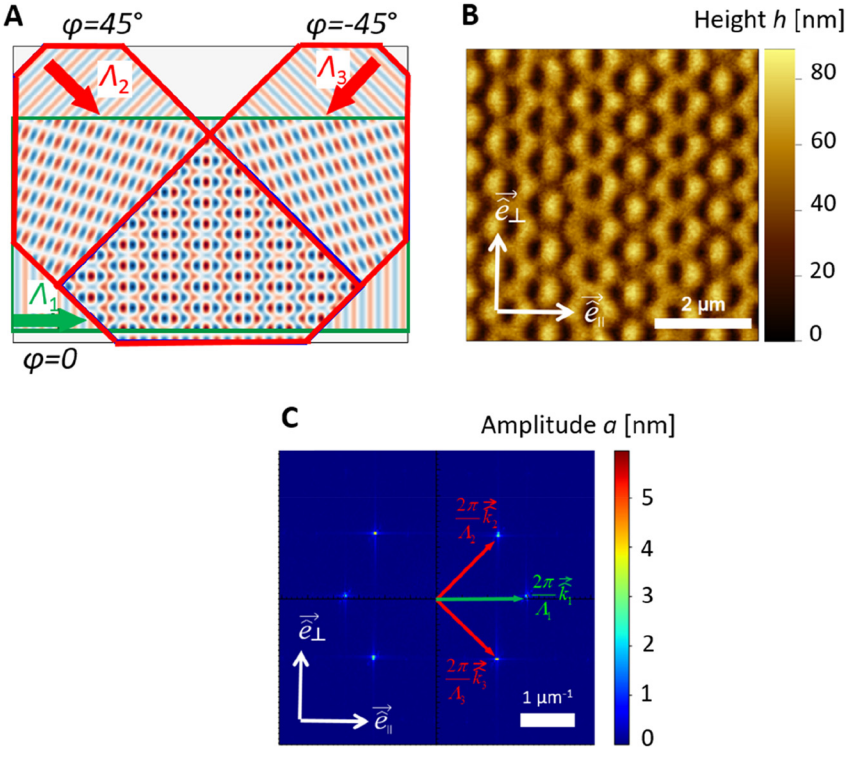


**Figure 2:** Designed MPG structure. (A) Orientation and periods of sequentially recorded overlaid sinusoidal corrugations by using UV-LIL method. (B) Measured topography of prepared MPG surface by AFM. (C) 2D FFT of the corrugation profile of the MPG structure. UV-LIL, UV-laser interference lithography; FFT, fast Fourier transform; AFM, atomic force microscopy.

corrugation depth of about 70 nm (difference in height of the topography) was observed, Figure 2B. The structure topography was further analyzed in more detail by 2D fast Fourier transform in order to reveal its periodic components. The obtained results are presented in Figure 2C, and they show clear peaks corresponding to recorded superimposed sinusoidal corrugations with periods $\Lambda_1$, $\Lambda_2$, and $\Lambda_3$. The dependence of the respective orientation of $\vec{k}_i$ vectors agrees with the azimuthal angles $\varphi$ used in the recording process. The modulation amplitude for each corrugation was determined to be around $a_1 = a_2 = a_3 = 8$ nm. This value is close to that used for the first order diffraction coupling to PSPs on the gold surface in the NIR part of the spectrum as shown before in literature [42].

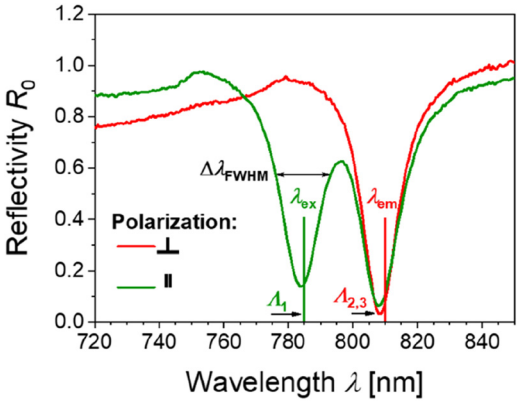


**Figure 3:** Plasmonic modes. Zero-order reflectivity spectrum measured for the normally incident beam at the MPG surface brought in contact with water ($n_s$ = 1.332).

## 3.2 Diffraction coupling to SPs by MPG

Periodically corrugated metallic surfaces allow for the phase matching of optical waves propagating in the far field with the near-field PSPs traveling along these surfaces. In general, the investigated geometry of MPG with multiple harmonic components allows fulfilling the phase-matching condition via its individual spectral components or their combination. For shallow corrugations, the wavelength-dependent propagation constant of PSPs in transverse magnetic polarization can be approximated by that for plane metal surface:

$$\vec{k}_{SP} = \frac{2\pi}{\lambda} Re\left\{\sqrt{\frac{n_m^2 \cdot n_s^2}{n_m^2 + n_s^2}}\right\}\left[\vec{e}_{\perp}\sin(\varphi) + \vec{e}_{\parallel}\cos(\varphi)\right], \quad (2)$$

where $n_m$ and $n_s$ are the refractive indices of the metal and the adjacent (water) dielectric, respectively, $\varphi$ is azimuthal angle, and $e \rightarrow \perp$ and $e \rightarrow \parallel$ are the unit orthogonal vectors in the plane of the MPG. The momentum of the incident beam becomes phase matched with that of PSPs when the following condition holds:

$$\pm\vec{k}_{SP} = \frac{2\pi}{\lambda} n_s \cos(\theta)\left[\vec{e}_{\perp}\sin(\varphi) + \vec{e}_{\parallel}\cos(\varphi)\right] + \sum_{i=1}^{3} m_i \frac{2\pi}{\Lambda_i}\vec{k}_i, \quad (3)$$

where $\theta$ and $\varphi$ are the polar and azimuthal angles, respectively, of a plane wave traveling in the dielectric with a refractive index $n_s$, $\Lambda_i$ is the period of corrugation components, $\vec{k}_i$ is unit vectors defining its orientation in the MPG plane ($i$ = 1, 2, 3), and integers ($m_1$, $m_2$, $m_3$) refer to a diffraction order.

The prepared gold-coated MPG structure was brought in contact with water exhibiting $n_s$ = 1.332, and the specular reflectivity spectrum $R_0$ was measured for the normally incident optical beam ($\theta = 0$, $\varphi$ is arbitrary). As seen in Figure 3, it exhibits two narrow dips centered at wavelengths of 784 and 817 nm and the coupling strength to shorter wavelength resonance can be controlled by the polarization of the incident optical beam. For the parallel polarization, the SPR at shorter wavelength is strongly pronounced, while when rotating the polarization to the perpendicular direction, it diminishes. The longer wavelength SPR dip is not sensitive to polarization changes. This behavior clearly relates to the fact that the short wavelength SPR originates from the diffraction on the corrugation component $\Lambda_1$ (which is recorded with only one azimuthal orientation) while the longer wavelength resonance is associated to the corrugation components $\Lambda_2$ and $\Lambda_3$ (forming a crossed grating with two identical orthogonal corrugations). The spectral position of shorter and longer wavelength resonances observed in the specular zero-order reflectivity spectrum ($R_0$) can be ascribed by using equation (3) to first-order diffraction coupling. The resonance at 785 nm is associated with the excitation of PSPs via the order (1,0,0) and the one at 810 nm to (0,1,0) and (0,0,1). Interestingly, the higher order coupling is not apparent in the visible-NIR spectral window of measured specular reflectivity $R_0$. It is worth of noting that the spectral position of short and long wavelength SPRs can be tuned by changing the respective periods $\Lambda_1$ and $\Lambda_2/\Lambda_3$ (see Figure S2A) and thus the reported MPG concept can be implemented for other emitters absorbing and emitting at different wavelengths $\lambda_{ab}$ and $\lambda_{em}$, respectively. Moreover, the coupling strength of PSPs with optical wave that impinges from the far field depends on the modulation depth $a_i$ and on the polarization of the incident field with respect to the grating vector as illustrated in Figure S2B.

## 3.3 Simulations of PEF on MPG

The MPG structure exhibits two distinct resonances that coincide with the absorption and emission wavelengths of the AF790 fluorophore $\lambda_{ab}$ and $\lambda_{em}$, respectively. The coupling of this fluorophore with the enhanced intensity of electric field $|\vec{E}|^2$ of resonantly excited PSPs at these wavelengths was studied using numerical simulations. The fluorophore was represented as an infinitesimally small electric dipole placed at a distance of 15 nm from the gold surface, which was chosen with respect to a typical immunoassay experiment considering the size of immunoglobulin G antibodies ($13.7 \times 8 \times 4$ nm [43]) and the fact that it is above the distance where strong quenching occurs [44]. The fluorescence emission has dipole characteristics [45, 46], and it cannot be excited when the orientation of the electric field $\vec{E}$ is perpendicular to the emitter absorption dipole $\vec{\mu}_{ab}$. In the reported experiments, fluorophores were conjugated to proteins by flexible molecular linkers with high degree of rotational freedom, which leads to randomizing its orientation in the fluorescence lifetime and consequently to an isotropic emission profile. Therefore, all possible orientations of the fluorophore absorption $\vec{\mu}_{ab}$ and emission $\vec{\mu}_{em}$ dipole were accounted for and averaged with respect to PSP electric field $\vec{E}$.

The excitation rate of a fluorophore is a function of the scalar product of the local electric field $\vec{E}$ at $\lambda_{ex}$ and absorption moment of the fluorophore $\vec{\mu}_{ab}$. Assuming the excitation rate is far below saturation, it can be expressed as $\propto|\vec{\mu}_{ab} \cdot \vec{E}|^2$ and thus being proportional to the electric field intensity enhancement $|\vec{E}/\vec{E}_0|^2$ accompanied with the resonant excitation of PSPs, which is strongest for the $\vec{E}$ component perpendicular to the surface. It reaches value $|\vec{E}|^2/|\vec{E}_0|^2 = 160$ (normalized with the intensity of the incident field intensity $|\vec{E}_0|^2$) for the resonant coupling of light to PSPs at $\lambda_{ex} = 785$ nm and the distance of 15 nm from the surface after the averaging along the structure corrugation (see Figure S3). This electric field intensity enhancement yields the mean amplification of the excitation rate of the emitter with randomly oriented absorption moment $\vec{\mu}_{ab}$ of 53, compared to an emitter in a homogeneous medium, which is similar to the excitation rate enhancement reported for excitation in attenuated total reflection (ATR) configuration with Kretschmann geometry [47].

After the PSP-enhanced excitation of the fluorophore at $\lambda_{ex}$, its emission can also be mediated by these modes at $\lambda_{em}$ as is analyzed further. These modes are generated upon the emission process by the near-field coupling and travel along the MPG surface. They become subsequently diffraction outcoupled to far-field waves that propagate away from its surface in the perpendicular direction. The emission characteristics mediated by the coupling to PSPs were averaged over all lateral positions and orientations of emission moment $\vec{\mu}_{em}$ (assuming rapid rotation of fluorophore on the surface within the lifetime of its excited state). As shown in the simulated angular distribution of fluorescence intensity emitted to the far field above the MPG in Figure 4A, it exhibits a pattern with multiple narrow dispersive bands that are attributed to first-order diffraction on the corrugation components $\Lambda_1$, $\Lambda_2$, and $\Lambda_3$, with corresponding diffraction order of (±1,0,0), (0,±1,0), and (0,0,±1), respectively. Clearly, these bands converge at the center, which consequently increases the probability of fluorescence emission to waves traveling at small polar angle $\theta$. Assuming a fluorescence collecting cone corresponding to a numerical aperture of 0.2, the MPG structure redirects the fluorescence light, so the detected intensity is enhanced by a factor of 8.2 with respect to a dipole in a homogeneous medium, where the emission is omnidirectional, and a factor of 6.2 compared to a dipole on a flat gold surface. MPG shows an additional 30% improvement compared to previous work utilizing a crossed grating

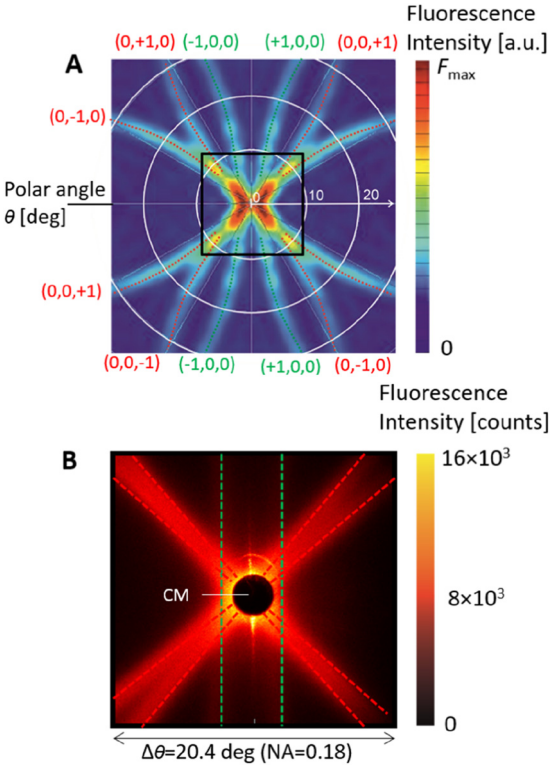


**Figure 4:** Surface plasmon-coupled emission at $\lambda_{em}$.
(A) Simulated and (B) measured angular distribution of fluorescence light emitted from MPG surface with indicated diffraction orders.

that was tuned to couple to plasmons at the excitation wavelength only [48].

## 3.4 Experimental observation of PEF on MPG

In order to measure the fluorescence signal amplified by the developed MPG nanostructure, its gold surface was modified with a mixed thiol SAM carrying OEG and COOH groups. The OEG thiol in the mixed thiol SAM was used to provide protection against unspecific binding of proteins present in analyzed liquid sample, and the smaller fraction of thiols carrying the COOH end group was employed for the post-modification of the sensor surface with functional groups.

Firstly, mouse IgG conjugated with AF790 was covalently bound to the COOH moieties on the surface by using the amine coupling, and the angular distribution of fluorescence light emitted from MPG was measured. This experiment was performed using an in-house-developed fluorescence reader configured to image the back focal plane of the objective lens placed before the sensor chip with MPG (lens 3 in Figure S4, back focal plane cuts the CM as indicated). The imaged angular distribution of emitted fluorescence light was measured by an EM-CCD detector in the range from $\theta = -10.2$ to 10.2°, Figure 4B. This image shows six dispersive bands originating from first-order outcoupling of PSP-mediated fluorescence emission at $\lambda_{em}$ at angles that agree with the simulations presented in Figure 4A.

Then, the configuration of the optical system of the reader was changed to image the surface of MPG to the EM-CCD detector to allow fluorescence readout of bioassays on the sensor chip. These measurements were carried out to evaluate the impact of individual components of the investigated MPG nanostructure to the fluorescence enhancement. The imaged area on the sensor chip was prepared so six different zones were coated with the same gold film and carrying the same surface density of IgG conjugated with AF790, see Figure 5A and D. The first reference zone was flat, the second and third zones were corrugated with only one component $\Lambda_2$ and $\Lambda_3$, the fourth and fifth zones carried two superimposed components $\Lambda_1$, $\Lambda_2$ and $\Lambda_1$, $\Lambda_3$, and the sixth zone comprised all components $\Lambda_1$, $\Lambda_2$, $\Lambda_3$ forming the full MPG structure. The sensor chip with all six zones carrying IgG-AF790 conjugates on their top was illuminated with a collimated and linearly polarized beam at $\lambda_{ex}$, and the intensity of emitted fluorescence light at $\lambda_{em}$ was collected and imaged to the EM-CCD detector. In order to distinguish between the impact of plasmonically enhanced excitation at $\lambda_{ex}$ and plasmon-coupled emission at $\lambda_{em}$, the polarization of the excitation beam was rotated so the SPR at the excitation wavelength $\lambda_{ex}$ was switched on and off (see Figure 3). The obtained fluorescence images are presented in Figure 5A–C. They show increased fluorescence signal in a circular illuminated area that is sliced to sections representing the six zones carrying different combinations of spatial components $\Lambda_1$, $\Lambda_2$, and $\Lambda_3$. The fluorescence intensity was averaged over the surface of each zone, and the value measured outside the illuminated area was subtracted in order to compensate for stray light and a dark signal of the EM-CCD detector. Then, the intensity from structured zones was normalized with that measured on a reference flat surface, and the obtained enhancement factors are summarized in the table included in Figure 5E.

For the perpendicular polarization of the excitation beam $\perp$ (which does not couple to surface PSPs at $\lambda_{ex}$ via corrugation component $\Lambda_1$), the impact of MPG to the SP-coupled emission at $\lambda_{em}$ was investigated. As Figure 5A shows, the presence of individual corrugations $\Lambda_2$ and $\Lambda_3$ provided the enhancement factor of collected fluorescence light intensity $F$ of 3.7. On the zones when these components are overlaid with $\Lambda_1$, this factor increases to 17, and when all the components $\Lambda_{1,2,3}$ are present, it raises to about 25. Let us note that the latter two enhancement values are substantially higher than the value predicted by simulations for the outcoupling of the emission occurring via PSPs at $\lambda_{em}$ (factor of 6.2). This observation can be attributed to partial miss alignment of the excitation beam polarization which leads to weak coupling to PSPs at the excitation wavelength $\lambda_{ex}$, which amends the excitation rate of the attached fluorophores. For the parallel polarization of the excitation beam $||$, the enhancement by individual corrugations $\Lambda_2$ and $\Lambda_3$ provided the same enhancement factor of 3.7. On the zones where these components are superimposed with $\Lambda_1$, the enhancement factor of 248 was measured, which is about 67 times higher than on the surface without this component and which agrees well with the predicted contribution of the enhanced excitation rate at $\lambda_{ex}$ of 53. On the zone where all components were present, additionally higher enhancement factor of 300 was determined with respect to the flat surface where both the excitation rate enhancement at $\lambda_{ex}$ by $\Lambda_1$ and the improving of collection yield at $\lambda_{em}$ by $\Lambda_2$ and $\Lambda_3$ are combined.

## 3.5 Readout of fluorescence immunoassay kinetics

The ability of the MPG nanostructure to enhance the performance characteristics of a fluorescence assay was

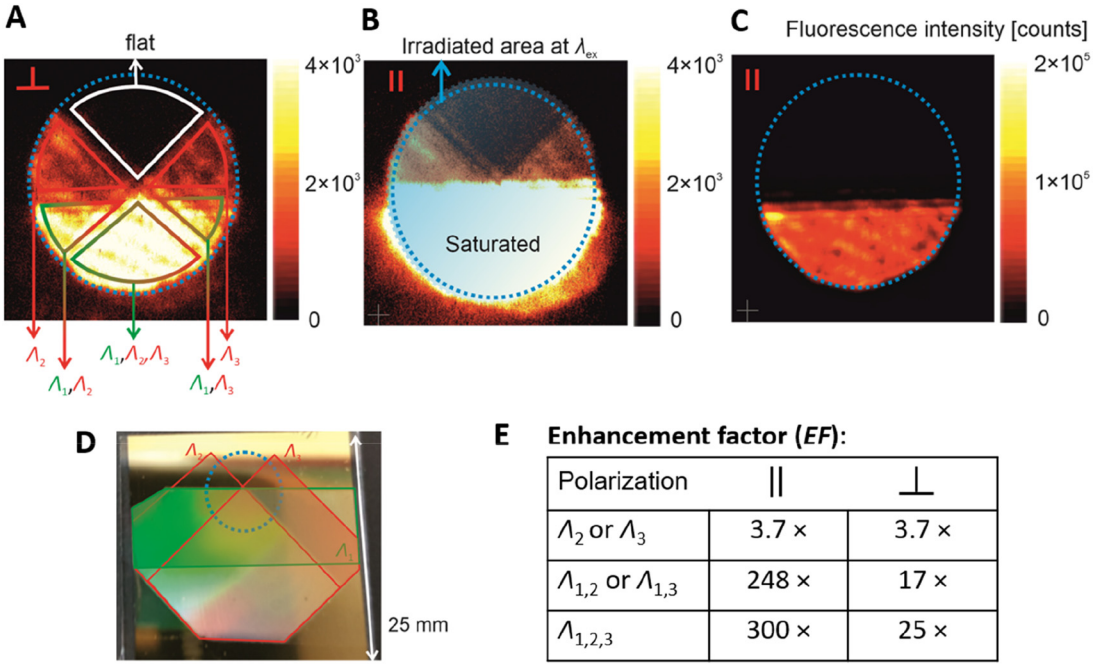


| Polarization | ∥ | ⊥ |
|---|---|---|
| $\Lambda_2$ or $\Lambda_3$ | 3.7 × | 3.7 × |
| $\Lambda_{1,2}$ or $\Lambda_{1,3}$ | 248 × | 17 × |
| $\Lambda_{1,2,3}$ | 300 × | 25 × |

**Figure 5:** Experimentally determined fluorescence enhancement factors. Fluorescence images taken from an area, where different combinations of spatial MPG components are present. Polarization of the excitation beam was (A) orthogonal and (B,C) parallel to the grating $\Lambda_1$. (D) Photograph of the prepared MPG with highlighted areas carrying different spectral components of MPG and (E) comparison of the respective enhancement factors with respect to that measured for the flat surface.

demonstrated for a microarray detection format. In this experiment, there was used the optical reader schematically shown in Figure 6A and a sensor chip with MPG nanostructure was interfaced with a flow-cell as indicated in Figure 6B. In this sensor configuration, the fluorescence signal $F$ was measured as a function of time $t$ from 21 circular spots defined on the sensor chip surface (see Figure S5). Each spot exhibited 220-μm diameter, and spot numbers 5, 8, 6, 9, 12, 10, 13, and 16 were defined on the sensor chip area in the flow cell chamber with the full MPG nanostructure coated with gold film. In addition, reference spots 1, 2, 3, 4, 7, 13, and 21 were placed outside the flow cell chamber, and reference spots 11, 15, 20, 14, 17, and 18 were defined inside the flow cell on the area with a flat gold film not carrying the MPG. The gold surface on the MPG inside the flow cell was functionalized by using the same mixed thiol SAM and amine-coupling strategy by mouse IgG molecules that were not labeled by a fluorophore. These biomolecules served as a ligand and allowed for affinity capture of target analyte (antimouse IgG conjugated with AF790) from the aqueous sample transported along the sensor surface through the flow cell chamber.

Initially, buffer was flowed through the sensor for at least 10 min until a stable baseline in the sensor response $F_b$ was established for all sensing spots 1–21. Afterward, a series of samples spiked with a target analyte (antimouse IgG conjugated with AF790) at concentrations between 10 fM and 10 nM was flowed over the sensor surface and its affinity binding at the array sensing spots was monitored through changes in the fluorescence signal $F$. The fluorescence signal deriving from each spot was averaged from the acquired images over its area and plotted by using in-house-developed LabView-based software. Variations in light source intensity were corrected by subtracting the signal of an illuminated reference spot outside the microfluidic channel from all other curves (spots 1, 2, 3, 4, 7, 13, and 21).

In a first step, the fluorescence signal was monitored for the affinity binding of high analyte concentrations (1 and 10 nM); therefore, the reader was configured for the monitoring of strong fluorescence intensities $F$ (intensity of the excitation beam irradiating the sensor chip surface at $\lambda_{ex}$ was 30 μW cm$^{-2}$, irradiation time of 0.3 s, with image accumulation of 10). Figure 7A compares the fluorescence signal kinetics $F(t)$ for two spots on the surface with gold MPG (red-colored curves) and two reference spots with flat gold surface (green-colored curves) where baseline signal $F_b$ was subtracted from the acquired signal. Each sample was flowed over the surface for 20 min followed by 10 min rinsing. These data reveal the affinity binding manifests itself as a gradual increase in the fluorescence signal $\Delta F$ until saturation is reached, then upon the rinsing step a

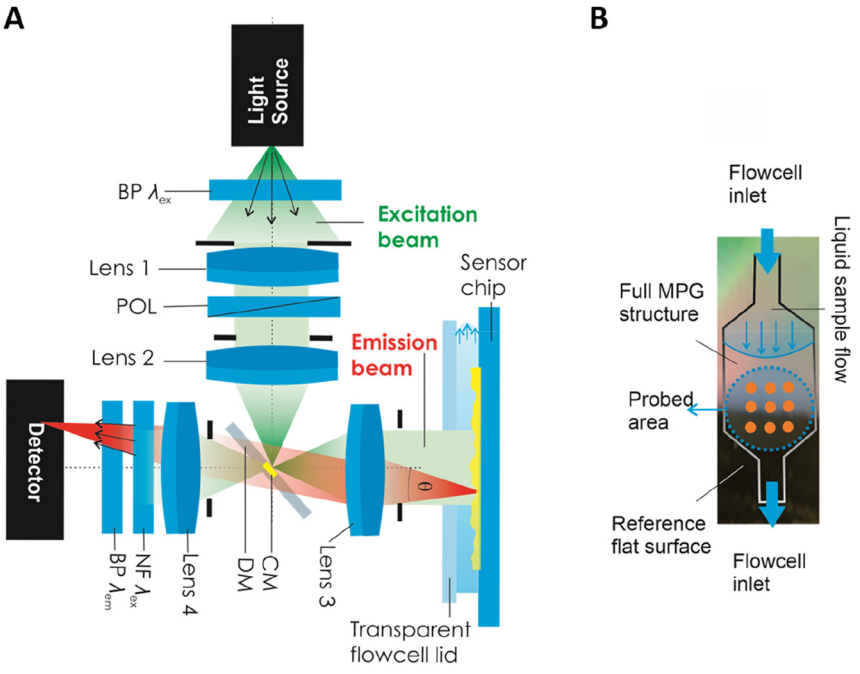


**Figure 6:** Optical biosensor reader. (A) Schematics of the optical configuration for the measurement of fluorescence signal kinetics from arrays of spots on the MPG sensor surface imaged to the detector. (B) Sensor chip with MPG structure that is interfaced with a flow cell and indication of the selected sensing spots. POL, polarizer; BP, bandpass filter; NF, notch filter; DM, dichroic mirror; CM, center mirror.

slow decrease in the fluorescence signal occurs due to dissociation of affinity bound molecules. The irradiation power at $\lambda_{ex}$ was selected to prevent the fluorophore labels from bleaching within the reaction time. The sensor response $\Delta F$ to the analyzed sample was defined as a difference in the fluorescence signal between the original baseline and after the 5 min rinsing. The measured data show that the MPG structure enhanced the fluorescence sensor response by a factor of 292 with respect to the flat surface, which is consistent with previous observations performed without the kinetics readout (see Figure 5).

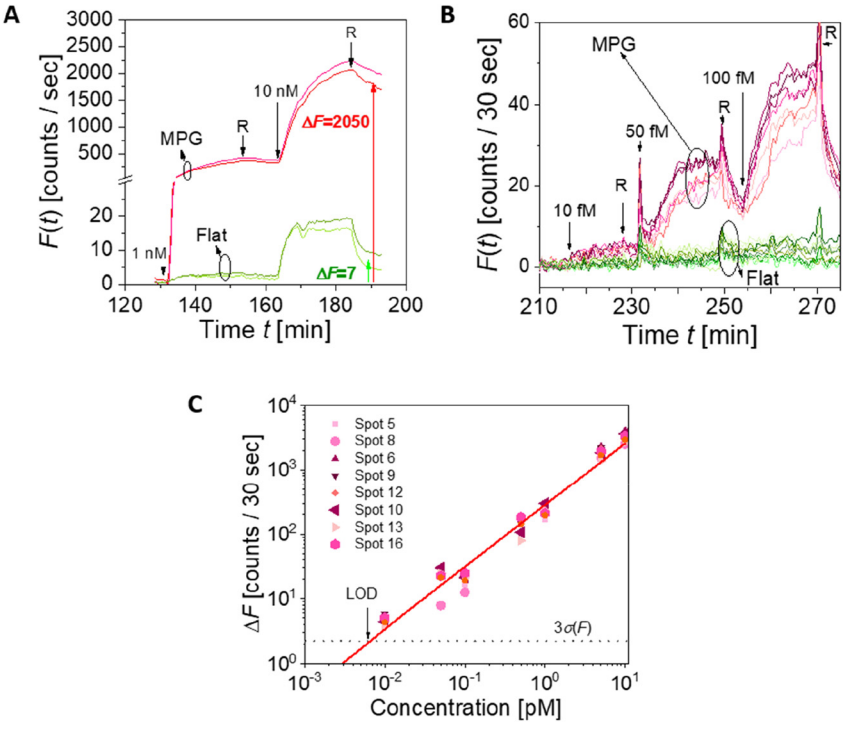


**Figure 7:** Biomolecular binding kinetics observed for a model IgG–anti-IgG on the MPG surface. The fluorescence reader was configured for detection of (A) high fluorescence intensities and (B) low fluorescence intensities for which the respective (C) calibration curve was established. The caption R states for the rinsing and red curves correspond to data measured on the MPG surface and green curves on the reference flat gold surface.

In a second step, the reader was configured for the monitoring of weak fluorescence signal in order to decrease the limit of detection (LOD) of the performed model assay (intensity of the excitation beam irradiating the sensor chip surface at $\lambda_{ex}$ was raised to 265 μW cm$^{-2}$, irradiation time 30 s, without accumulation of images). In Figure 7B, the kinetic measurement of the fluorescence signal $F(t)$ for the target analyte concentrations of 10, 50, and 100 fM is shown. For the spots on the nonstructured reference area (green-colored curves), no measurable change in signal was observed, while on the area structured with gold MPG, a clear increase in $F(t)$ for all shown concentrations is detected. The kinetics of the reaction presented in Figure 7B is qualitatively different from that in Figure 7A. The fluorescence signal intensity $F(t)$ faster saturates at already low concentrations where only a small fraction of available binding sites is occupied by the target analyte conjugated with AF790 and it also faster decreases upon the rising step. These effects are caused by the more pronounced bleaching occurring due to the more intense irradiation power at $\lambda_{ex}$.

From the measured kinetic data, the calibration curve presented in Figure 7C was established and the respective LOD was determined. The fluorescence response $\Delta F$ on the MPG structure was plotted against the analyte concentrations of 10 fM, 50 fM, 100 fM, 0.5 pM, 1 pM, and 5 pM in log-log scale and fitted by a linear function with a slope $S$ = 0.95 counts/30 s/fM. The LOD was determined from the intersection of the fitted calibration curve with three times the standard deviation of the fluorescence background $3\sigma(F)$, where $\sigma(F)$ = 0.75 counts/30 s. The achieved (average) LOD is 6 fM for the used measuring spot numbers 5, 8, 6, 9, 12, 10, 13, and 16. It should be noted that the imaged area of 4 × 4 mm can accommodate up to 270 of these spots, which can be used for parallel monitoring of biomolecular binding kinetics undisturbed by the background signal originating from the bulk, owing to the local enhancement of emitted fluorescence signal at the sensor chip surface.

# 4 Conclusions

A novel metallic nanostructure with a delocalized plasmonic hotspot and multiple SPR wavelengths is reported and its tailoring for PEF is discussed. It is based on a MPG that supports series of spectrally narrow (15 nm width) resonances associated with the diffraction coupling to PSP modes. These substrates were utilized for fluorescence immunoassay measurements, which show an enhancement factor of 300× on the MPG surface with respect to a nonstructured surface carrying the same biointerface architecture. This enhancement factor is about 2× as high as previously reported by our group for single period crossed grating tuned for the excitation enhancement only [48] and more than 5× higher than what has been reported for PEF with the ATR method and Kretschmann configuration [49]. In conjunction with a reader allowing spatially resolved monitoring of fluorescence intensity from multiple spots arranged in a footprint of 16 mm$^2$, there is demonstrated the possibility of highly parallelized measurement of affinity binding kinetics that is not masked by the background single originating from the bulk and with high sensitivity enabling reaching the LOD of 6 fM. The reported LOD is about 66× improved compared to similar assays reported by our previous work on single period crossed gratings and ATR-based PEF [49]. By changing the periods of the superimposed periodic structures, the proposed MPG concept can be utilized for arbitrary emitters in the red and infrared part of the spectrum (for a gold surface) or at shorter wavelengths (for silver or aluminum) covering a wide range of available fluorophore labels. In addition, the ability to translate the MPG preparation process to mass production compatible technologies such as UV-NIL in roll-to-roll format in conjunction with deploying of novel antifouling biointerface architectures [50] may open a pathway for future industrial applications (including analysis of trace amounts of diseases biomarkers in bodily fluids, which is a topic for the follow-up work).

# Abbreviations

| | |
|---|---|
| AF790 | Alexa Fluor 790 fluorescent dye |
| CM | Central mirror |
| DM | Dichroic mirror |
| EBL | Electron beam lithography |
| LIL | Laser interference lithography |
| LSP | Localized surface plasmon |
| MPG | Multi-period plasmonic grating |
| NA | Numerical aperture |
| PEF | Plasmon-enhanced fluorescence |
| PSP | Propagating surface plasmon |
| SAM | Self-assembled monolayer |
| SP | Surface plasmon |
| SPR | Surface plasmon resonance |
| UV-NIL | UV-nanoimprint lithography |
| UV-LIL | UV-laser interference lithography |

**Author contribution**: All the authors have accepted responsibility for the entire content of this submitted manuscript and approved submission.

**Research funding**: S.F., S.H., S.M. E.M., and J.D. received support from the European Union's Horizon 2020 research and the innovation program under Grant agreement no.

633937, project ULTRAPLACAD. In addition, S.H., S.F., and J.D. were partially supported by the Austrian Research Promotion Agency (FFG) with Grant agreement no. 861578 (ERANET project PLABAN), and J.D. acknowledges support from the ESIF and MEYS (Project 'FZU researchers, technical and administrative staff mobility' – CZ.02.2.69/ 0.0/ 0.0/18_053/0016627).

**Conflict of interest statement**: The authors declare no conflicts of interest regarding this article.

## References

[1] B. Liedberg, C. Nylander, and I. Lunström, "Surface plasmon resonance for gas detection and biosensing," *Sens. Actuators*, vol. 4, pp. 299–304, Jan. 1983.

[2] J. Homola, *Surface Plasmon Resonance Based Sensors*, 2006.

[3] M. F. Cardinal, E. Vander Ende, R. Hackler, et al., "Expanding applications of SERS through versatile nanomaterials engineering," *Chem. Soc. Rev.*, vol. 46, no. 13, pp. 3886–3903, 2017.

[4] Y. Jeong, Y. M. Kook, K. Lee, and W. G. Koh, "Metal enhanced fluorescence (MEF) for biosensors: general approaches and a review of recent developments," *Biosens. Bioelectron.*, 2018. https://doi.org/10.1016/j.bios.2018.04.007.

[5] M. Li, S. K. Cushing, and N. Wu, "Plasmon-enhanced optical sensors: a review," *Analyst*, vol. 140, no. 2, pp. 386–406, 2015.

[6] G. W. Ford and W. H. Weber, "Electromagnetic interactions of molecules with metal surfaces," *Phys. Rep.*, vol. 113, no. 4, pp. 195–287, 1984.

[7] J. R. Lakowicz, K. Ray, M. Chowdhury, H. Szmacinski, Y. Fu, J. Zhang, and K. Nowaczyk, "Plasmon-controlled fluorescence: a new paradigm in fluorescence spectroscopy," *Analyst*, vol. 133, no. 10, pp. 1308–1346, 2008.

[8] E. Fort and S. Grésillon, "Surface enhanced fluorescence," *J. Phys. D Appl. Phys.*, vol. 41, no. 1, p. 013001, 2008.

[9] J. R. Lakowicz, K. Ray, M. Chowdhury et al., "Plasmon-controlled fluorescence: a new paradigm in fluorescence spectroscopy," *Analyst*, vol. 133, no. 10, pp. 1308–1346, 2008.

[10] F. D. Stefani, K. Vasilev, N. Bocchio, N. Stoyanova, and M. Kreiter, "Surface-plasmon-mediated single-molecule fluorescence through a thin metallic film," *Phys. Rev. Lett.*, vol. 94, no. 2, pp. 1–4, 2005.

[11] B. Auguié and W. L. Barnes, "Collective resonances in gold nanoparticle arrays," *Phys. Rev. Lett.*, vol. 101, no. 14, p. 143902, Sep. 2008.

[12] M. Bauch and J. Dostalek, "Collective localized surface plasmons for high performance fluorescence biosensing," *Opt. Express*, vol. 21, no. 17, p. 20470, Aug. 2013.

[13] E. Petryayeva and U. J. Krull, "Localized surface plasmon resonance: nanostructures, bioassays and biosensing-A review," *Anal. Chim. Acta*, vol. 706, no. 1, pp. 8–24, 2011.

[14] Y. Chen, K. Munechika, and D. S. Ginger, "Dependence of fluorescence intensity on the spectral overlap between fluorophores and plasmon resonant single silver nanoparticles," *Nano Lett.*, vol. 7, no. 3, pp. 690–696, Mar. 2007.

[15] G. Vecchi, V. Giannini, and J. Gómez Rivas, "Shaping the fluorescent emission by lattice resonances in plasmonic crystals of nanoantennas," *Phys. Rev. Lett.*, vol. 102, no. 14, Apr. 2009, https://doi.org/10.1103/physrevlett.102.146807.

[16] Y. Wang, L. Wu, T.I. Wong, et al., "Directional fluorescence emission co-enhanced by localized and propagating surface plasmons for biosensing," *Nanoscale*, vol. 8, no. 15, pp. 8008–8016, Apr. 2016.

[17] V. G. Kravets, A. V. Kabashin, W. L. Barnes, and A. N. Grigorenko, "Plasmonic surface lattice resonances: a review of properties and applications," *Chem. Rev.*, vol. 118, pp. 1–72, 2018.

[18] P. Biagioni, J.-S. Huang, and B. Hecht, "Nanoantennas for visible and infrared radiation," *Reports Prog. Phys.*, vol. 75, no. 2, p. 024402, Feb. 2012.

[19] A. Devilez, B. Stout, and N. Bonod, "Compact metallo-dielectric optical antenna for ultra directional and enhanced radiative emission," *ACS Nano*, vol. 4, no. 6, pp. 3390–3396, Jun. 2010.

[20] T. Coenen, E. J. R. Vesseur, A. Polman, and A. F. Koenderink, "Directional emission from plasmonic Yagi-Uda antennas probed by angle-resolved cathodoluminescence spectroscopy," *Nano Lett.*, vol. 11, no. 9, pp. 3779–3784, Sep. 2011.

[21] T. Kosako, Y. Kadoya, and H. F. Hofmann, "Directional control of light by a nano-optical Yagi-Uda antenna," *Nat. Photonics*, vol. 4, no. 5, pp. 312–315, May 2010.

[22] A. B. Taylor and P. Zijlstra, "Single-molecule plasmon sensing: current status and future prospects," *ACS Sensors*, vol. 2, no. 8. American Chemical Society, pp. 1103–1122, Aug. 2017.

[23] J. R. Lakowicz, J. Malicka, I. Gryczynski, and Z. Gryczynski, "Directional surface plasmon-coupled emission: a new method for high sensitivity detection," *Biochem. Biophys. Res. Commun.*, vol. 307, no. 3, pp. 435–439, 2003.

[24] I. I. Smolyaninov, Y. J. Hung, and C. C. Davis, "Fluorescence enhancement by surface gratings," *Opt. InfoBase Conf. Pap.*, vol. 14, no. 22, pp. 10825–10830, 2007.

[25] A. Nicol and W. Knoll, "Characteristics of fluorescence emission excited by grating-coupled surface plasmons," *Plasmonics*, vol. 13, no. 6, pp. 2337–2343, 2018.

[26] K. Tawa, H. Hori, K. Kintaka, K. Kiyosue, Y. Tatsu, and J. Nishii, "Optical microscopic observation of fluorescence enhanced by grating-coupled surface plasmon resonance," *Opt. Express*, vol. 16, no. 13, p. 9781, Jun. 2008.

[27] E. Prodan, "A hybridization model for the plasmon response of complex nanostructures," *Science (80-.)*, vol. 302, no. 5644, pp. 419–422, Oct. 2003.

[28] S. A. Safiabadi Tali and W. Zhou, "Multiresonant plasmonics with spatial mode overlap: overview and outlook," *Nanophotonics*, vol. 8, no. 7, pp. 1199–1225, Jul. 2019.

[29] J. Parsons, E. Hendry, C. P. Burrows, B. Auguié, J. R. Sambles, and W. L. Barnes, "Localized surface-plasmon resonances in periodic nondiffracting metallic nanoparticle and nanohole arrays," *Phys. Rev. B Condens. Matter Mater. Phys.*, vol. 79, no. 7, 2009, https://doi.org/10.1103/physrevb.79.073412.

[30] J. S. Pang, I. G. Theodorou, A. Centeno, et al., "Tunable three-dimensional plasmonic arrays for large near-infrared fluorescence enhancement," *ACS Appl. Mater. Interfaces*, vol. 11, no. 26, 23083–23092, Jul. 2019.

[31] K. M. McPeak, S. V. Jayanti, S. J. P. Kress, et al., "Plasmonic films can easily be better: rules and recipes," *ACS Photonics*, vol. 2, no. 3, pp. 326–333, 2015.

[32] R. Gupta, M. J. Dyer, and W. A. Weimer, "Preparation and characterization of surface plasmon resonance tunable gold and

silver films," *J. Appl. Phys.*, vol. 92, no. 9, pp. 5264–5271, Nov. 2002.
[33] B. Ai, Y. Yu, H. Möhwald, G. Zhang, and B. Yang, "Plasmonic films based on colloidal lithography," *Adv. Colloid Interface Sci.*, vol. 206. Elsevier B.V., pp. 5–16, 2014.
[34] T. H. P. Chang, M. Mankos, K. Y. Lee, and L. P. Muray, "Multiple electron-beam lithography," *Microelectron. Eng.*, vols. 57–58, pp. 117–135, Sep. 2001.
[35] C. Lu and R. H. Lipson, "Interference lithography: a powerful tool for fabricating periodic structures," *Laser Photonics Rev.*, vol. 4, no. 4, pp. 568–580, 2010.
[36] A. Rodriguez, A. Echeverría, M. Ellman, et al., "Laser interference lithography for nanoscale structuring of materials: from laboratory to industry," *Microelectron. Eng.*, vol. 86, nos. 4–6, pp. 937–940, Apr. 2009.
[37] H. Schift, "Nanoimprint lithography: an old story in modern times? A review," *J. Vac. Sci. Technol. B Microelectron. Nanom. Struct.*, vol. 26, no. 2, pp. 458–480, Mar. 2008.
[38] S. V. Sreenivasan, "Nanoimprint lithography steppers for volume fabrication of leading-edge semiconductor integrated circuits," *Microsyst. Nanoeng.*, vol. 3, no. 1, pp. 1–19, 2017.
[39] N. Kooy, K. Mohamed, L. T. Pin, and O. S. Guan, "A review of roll-to-roll nanoimprint lithography," *Nanoscale Res. Lett.*, vol. 9, no. 1, pp. 1–13, Jun. 2014.
[40] I. Khan, H. Keshmiri, F. Kolb, T. Dimopoulos, E. J. W. List-Kratochvil, and J. Dostalek, "Multidiffractive broadband plasmonic absorber," *Adv. Opt. Mater.*, vol. 4, no. 3, pp. 435–443, 2016.
[41] K. Jans, K. Bonroy, K. De Palmas, et al., "Stability of mixed PEO–thiol SAMs for biosensing applications," *Langmuir*, vol. 24, no. 8, pp. 3949–3954, 2008.
[42] P. Adam, J. Dostálek, and J. Homola, "Multiple surface plasmon spectroscopy for study of biomolecular systems," *Sens. Actuators B Chem.*, vol. 113, no. 2, pp. 774–781, Feb. 2006.
[43] Y. H. Tan, M. Liu, B. Nolting, J. G. Go, J. Gervay-Hague, and G. Liu, "A nanoengineering approach for investigation and regulation of protein immobilization," *ACS Nano*, vol. 2, no. 11, pp. 2374–2384, Nov. 2008.
[44] K. Sergelen, S. Fossati, A. Turupcu, et al., "Plasmon field-enhanced fluorescence energy transfer for hairpin aptamer assay readout," *ACS Sensors*, vol. 2, no. 7, pp. 916–923, 2017.
[45] F. Michelotti and E. Sepe, "Anisotropic fluorescence emission and photobleaching at the surface of one-dimensional photonic crystals sustaining Bloch surface waves. I. Theory," *J. Phys. Chem. C*, vol. 123, no. 34, pp. 21167–21175, Aug. 2019.
[46] E. Sepe, A. Sinibaldi, N. Danz, P. Munzert, and F. Michelotti, "Anisotropic fluorescence emission and photobleaching at the surface of one-dimensional photonic crystals sustaining Bloch surface waves. II. Experiments," *J. Phys. Chem. C*, vol. 123, no. 34, pp. 21176–21184, Aug. 2019.
[47] M. Bauch, K. Toma, M. Toma, Q. Zhang, and J. Dostalek, "Plasmon-enhanced fluorescence biosensors: a review," *Plasmonics*, vol. 9, no. 4, pp. 781–799, Aug. 2014.
[48] M. Bauch, S. Hageneder, and J. Dostalek, "Plasmonic amplification for bioassays with epi-fluorescence readout," *Opt. Express*, vol. 22, no. 26, p. 32026, 2014.
[49] S. Hageneder, M. Bauch, and J. Dostalek, "Plasmonically amplified bioassay - total internal reflection fluorescence vs. epifluorescence geometry," *Talanta*, vols. 156–157, pp. 225–231, Aug. 2016.
[50] D. Kotlarek, M. Vorobii, W. Ogieglo, W. Knoll, C. Rodriguez-Emmenegger, and J. Dostálek, "Compact grating-coupled biosensor for the analysis of thrombin," *ACS Sensors*, vol. 4, no. 8, pp. 2109–2116, 2019.

**Supplementary material:** The online version of this article offers supplementary material (https://doi.org/10.1556/nanoph-2020-0270).